Published in final edited form as:
J Nucl Med. 2009 November ; 50(11): 1873–1880. doi:10.2967/jnumed.109.067140.

Targeting the $\alpha_v\beta_3$ Integrin for Small-Animal PET/CT of Osteolytic Bone Metastases

Thaddeus J. Wadas[1], **Hongju Deng**[2], **Jennifer E. Sprague**[1,3], **Alexander Zheleznyak**[1], **Katherine N. Weilbaecher**[2], and **Carolyn J. Anderson**[1,4,5]

[1]Mallinckrodt Institute of Radiology, Washington University School of Medicine, St. Louis, Missouri

[2]Department of Medicine, Washington University School of Medicine, St. Louis, Missouri

[3]Edward Mallinckrodt Department of Pediatrics, Washington University School of Medicine, St. Louis, Missouri

[4]Department of Biochemistry and Molecular Biophysics, Washington University School of Medicine, St. Louis, Missouri

[5]Department of Chemistry, Washington University, St. Louis, Missouri

Abstract

This article describes the evaluation of the radiopharmaceutical ^{64}Cu-CB-TE2A-c(RGDyK) (^{64}Cu-RGD) as an imaging agent for osteolytic bone metastases and their associated inflammation by targeting of the $\alpha_v\beta_3$ integrin on osteoclasts and the proinflammatory cells involved at the bone metastatic site.

Methods—The ^{64}Cu-RGD radiotracer was evaluated in the transgenic mouse expressing Tax (Tax$^+$), which spontaneously develops osteolytic tumors throughout the vertebrae and hind limbs, using biodistribution studies and small-animal PET/CT. Histologic analysis was also performed on Tax$^+$ mouse tails, using hematoxylin and eosin and tartrate-resistant acid phosphatase to confirm the presence of osteolytic bone lesions and the presence of osteoclasts, respectively. Additionally, a proof-of-principle study was conducted with a small group of Tax$^+$ animals presenting with osteolytic lesions. These animals were treated with the bisphosphonate zoledronic acid and imaged with ^{64}Cu-RGD to determine whether this radiopharmaceutical was sensitive enough to detect a response to the bisphosphonate therapy.

Results—Biodistribution studies using ^{64}Cu-RGD demonstrated that Tax$^+$ mice between the ages of 6 and 12 mo had a greater accumulation of activity in their tail vertebrae than did the wild-type (WT) cohort ($P = 0.013$). Additionally, Tax$^+$ mice between the ages of 6 and 12 mo had significantly more tracer activity associated with their tail vertebrae than did Tax$^+$ mice older than 12 mo ($P = 0.003$), suggesting that earlier bone metastases cause an increased recruitment of $\alpha_v\beta_3$-expressing cells. Small-animal PET/CT with ^{64}Cu-RGD was conducted on Tax$^+$ and WT mice. On the basis of standardized uptake value analysis, Tax$^+$ mice had approximately 2-fold more tail-associated activity than did WT animals ($P = 0.0157$). Additionally, decreases in uptake were observed in the tails of Tax$^+$ mice after treatment with the osteoclast inhibitor zoledronic acid, and histologic analysis of Tax$^+$ mouse-tail vertebrae revealed the presence of Tax$^+$ tumor cells, osteoclasts, and proinflammatory cells within the bone microenvironment.

For correspondence or reprints contact: Carolyn J. Anderson, Mallinckrodt Institute of Radiology, Washington University School of Medicine, 510 S. Kingshighway Blvd., Campus Box 8225, St. Louis, MO 63110. andersoncj@wustl.edu.

Conclusion—Together, these data suggest that ^{64}Cu-RGD has the potential to effectively image osteolytic bone metastases and monitor the physiologic changes in the bone metastatic microenvironment after osteoclast-inhibiting bisphosphonate therapy.

Keywords

bone; metastasis; integrin; PET; bisphosphonate

Bone metastases are a debilitating form of metastases causing severe bone pain, hypercalcemia, and pathologic bone fracture, and in some cases paralysis. Although the number of Americans living with bone metastases is unknown, it is estimated that at least 25% of those who die of cancer have them at the time of death (1). Bone metastases are classified as either osteoblastic or osteolytic lesions. The former results from the stimulation and proliferation of osteoblasts and culminates in the formation of excess bone. Conversely, osteolytic lesions are caused by the vicious cycle of bidirectional interactions between tumor cells and osteoclasts. In this cycle, increased numbers of osteoclasts attach to the bone matrix via the $\alpha_v\beta_3$ integrin. After attachment, an acidic environment that dissolves the underlying bone matrix is created by the osteoclasts. This destruction releases important growth factors from the bone matrix, which stimulate tumor cell growth and proliferation into the recently created space within the bone (1).

To assist clinicians, several imaging modalities exist that have been used to detect the presence of bone metastases, but each modality has specific limitations when attempting to detect osteolytic bone lesions (2). Visualization of osteolytic metastases using radiography is difficult because 30%–75% of normal bone mineral content must be lost before osteolytic lesions can be detected. Skeletal scintigraphy (SS), another imaging modality, is the most commonly used means of detecting bone metastases and uses radiopharmaceutical contrast agents such as ^{99m}Tc-methylene diphosphonate. Although SS is more sensitive than radiography, it is reported to have lower specificity and, importantly, cannot be used to monitor a patient's response to therapy because tumor progression and bone healing are virtually indistinguishable in images obtained by this method. Additionally, it is ineffective at imaging the purely osteolytic lesions associated with multiple myeloma, and false-positive results due to fracture are often observed. CT is a highly sensitive modality, though it lacks the ability to scan large anatomic areas in a single imaging session. MRI, which is an imaging modality that relies on a powerful magnetic field to provide detailed images of the bone and bone marrow, cannot detect the destruction of bone structure because cortical bone does not produce a signal and appears black on T1- and T2-weighted sequences. In addition, like CT, MRI lacks the ability to scan large anatomic areas in a single imaging session. SPECT can also be used to detect bone lesions but relies on the same radiopharmaceuticals as SS and thus has better detection capabilities for osteoblastic lesions.

PET, which is an imaging modality that uses positron-emitting radiopharmaceuticals such as ^{18}F-FDG and ^{18}F-fluoride, is currently more specific and better at detecting osteolytic bone lesions than the former imaging modalities. However, diagnoses rely on the uptake of ^{18}F-FDG, which is a nonspecific marker for tumor metabolism or the preferential deposition of ^{18}F at sites of bone remodeling and turnover, respectively (3). Both false-negative and false-positive observations have occurred with ^{18}F-FDG imaging of osteolytic bone metastases, with false-negative results caused by low uptake in bone and false-positive results attributed to increased ^{18}F-FDG uptake in inflamed tissue and areas of wound healing (4–6).

The development of biomarkers that will help physicians accurately diagnose and therapeutically target osteolytic bone metastases would be of value in a clinical setting. Current work has been directed toward the development of imaging and therapeutic agents such as

bisphosphonates that directly target osteoclasts or substances that disrupt bone resorption mechanisms by inhibiting the action of biomolecules such as receptor activator for nuclear factor κ B ligand and cathepsin K (7–12). The $\alpha_v\beta_3$ integrin is another biomolecule that can be exploited to target osteoclasts through imaging and therapy. The $\alpha_v\beta_3$ integrin is expressed on many tumor cell types, has been shown to play a role in cancer metastasis, and is abundantly expressed on osteoclasts (13–16). In addition, the $\alpha_v\beta_3$ integrin has been imaged successfully in angiogenic and cancer models using ligands containing the amino acid sequence arginine-glycine-aspartic acid (RGD) (17–19). Moreover, osteoclasts have been successfully imaged using a ^{64}Cu-labeled RGD radiopharmaceutical (Fig. 1A) that targets the $\alpha_v\beta_3$ integrin in a pharmacologically induced model of osteolysis (20). Sprague et al. demonstrated that specific uptake of the radiopharmaceutical ^{64}Cu-RGD was observed in osteoclasts but not in bone marrow macrophages (20). In addition to cell uptake studies, biodistribution studies of mice injected at the mouse calvarium with parathyroid hormone demonstrated significantly increased uptake of ^{64}Cu-RGD only at the calvarium when compared with the group treated with saline. This finding was corroborated by small-animal PET, which showed increased radiopharmaceutical uptake in the calvarium of the parathyroid hormone–treated mice, whereas a similar increase was not observed in the saline-treated group. These studies demonstrated that increased numbers of osteoclasts can be imaged successfully using ^{64}Cu-RGD and PET. This report investigates ^{64}Cu-RGD as an imaging agent for osteolytic bone destruction and associated inflammation that occurs in bone metastases in a Tax-expressing transgenic mouse model (Tax$^+$) of spontaneous, osteolytic metastatic disease, which mimics human osteolytic disease in malignancies such as adult T-cell leukemia lymphoma and multiple myeloma.

MATERIALS AND METHODS

All work involving the use of radioactive materials at Washington University is conducted under the authorization of the Radiation Safety Committee in accordance with the University's Nuclear Regulatory Commission license. ^{64}Cu (half-life, 12.7 h; β^+, 17.8%; $E_{\beta+\ max}$, 656 keV; β^-, 38.4%; $E_{\beta-\ max}$, 573 keV) (21) was produced on a biomedical cyclotron (CS-15; Cyclotron Corp.) at Washington University School of Medicine (22). All other chemicals were purchased from Sigma-Aldrich Chemical Co., and solutions were prepared using ultrapure water (18 MΩ-cm resistivity). Zoledronic acid (ZA) (as the hydrated disodium salt) was provided by Novartis Pharma AG. The chelator CB-TE2A and CB-TE2A-c(RGDyK) were prepared according to previously published procedures (20,23). Radiochemistry reaction progress and purity were monitored by analytic radio–thin-layer chromatography (radio-TLC), which was conducted on a Bioscan AR 2000 radio-TLC scanner equipped with a 10% methane:argon gas supply and a PC interface running Winscan (version 3; Academic Software, Inc.) analysis software. C-18 plates were used with an eluent mixture of 3:7 10% NH_4OAc:MeOH and the complex $^{64}Cu(OAc)_2$ as a standard control. Radioactive samples were counted using a Beckman 8000 automated well-type γ-counter. The PET and CT data were acquired using either a microPET Focus 120 or a microPET Focus 220 and a microCAT II system, respectively. All systems were purchased from Siemens Medical Solutions USA.

Animal Handling

Transgenic mice that expressed HTLV-1 Tax under the human granzyme B promoter (Tax$^+$ C57B6/SJL) have been previously described (24). Mice were housed under pathogen-free conditions according to the guidelines of the Division of Comparative Medicine, and the Animal Studies Committee of Washington University School of Medicine approved all experiments.

Radiochemistry

The complexation of 64Cu to CB-TE2A-c(RGDyK) was achieved by reacting 2 μg (1.3×10^{-3} μmol) of CB-TE2A-c(RGDyK), a 118-μL solution of 0.1 M NH_4OAc (pH 8.0), and 37 MBq (1,000 μCi) of $^{64}CuCl_2$ in 0.1N HCl for 1.5 h at 95°C. If needed, the reaction was further purified using a previously published method (25). After purification, purity was greater than 95% based on radio-TLC analysis, and the specific activities ranged from 11 to 37 MBq/μg (300–1,000 μCi/μg).

Biodistribution Studies

Biodistribution studies were conducted as previously described (26,27). Briefly, Tax^+ mice (6–15 mo) were injected with ^{64}Cu-RGD (0.74 MBq (27 μCi) in 150 μL/mouse) via a femoral vein catheter. Animals were sacrificed at selected times after injection, and organs of interest were removed, weighed, and counted on a Beckman γ-counter 8000. The percentage injected dose per gram (%ID/g) and percentage injected dose per organ were calculated by comparison to a weighed, counted standard.

Serum Tartrate-Resistant Acid Phosphatase (TRAP) Analysis

Blood samples were collected from mice via submandibular venous puncture and placed in serum separator tubes (Becton Dickinson). The blood samples were placed at 4°C for 5 min, and then centrifuged at 10,000 rpm for 5 min. The serum was separated from the cellular fraction and stored at 0°C. Levels of TRAP 5b were determined using a TRAP 5b enzyme-linked immunosorbent assay system (IDS) according to the manufacturer's instructions. Samples were run in triplicate.

Small-Animal PET/CT

Transgenic HTLV-1 Tax^+ mice were injected with 6–11 MBq (200–400 μCi) of ^{64}Cu-RGD via the femoral vein catheter. Tails were imaged using small-animal PET/CT at 1 h after injection in the same bed position. Coregistered images were generated using ordered-subset expectation maximization (OSEM) reconstruction techniques, regions of interest were drawn using the open-source software program AMIDE, and standardized uptake values (SUVs) were determined using the formula SUV = [(nCi/mL) × (animal weight (g))/injected dose (nCi)].

Bisphosphonate Therapy Response Imaging

Tax^+ mice were injected with 6–11 MBq (200–400 μCi) of ^{64}Cu-RGD. Tails were imaged using small-animal PET/CT at 1 h after injection in the same bed position. Twenty-four hours after imaging, mice were given 1 dose of ZA (0.75-μg dose, ~30 μg/kg) via intraperitoneal injection. A second intraperitoneal dose was administered 7 d later. This ZA dosing schedule was designed to produce drug levels similar to those achieved in clinical regimens for the treatment of bone metastases. After the second treatment, mice were injected with 6–11 MBq of ^{64}Cu-RGD and imaged as previously described. Coregistered images were generated using OSEM reconstruction techniques, regions of interest were drawn using the software program AMIDE, and standardized uptake values (SUVs) were determined using the formula SUV = [(nCi/mL) × (animal weight (g))/injected dose (nCi)].

Histology

Mouse tails were fixed in formalin, decalcified in 14% ethylene diaminetetraacetic acid, paraffin-embedded, and stained with hematoxylin and eosin and for TRAP. Images were visualized under a Nikon Eclipse TE300 microscope equipped with a Plan Fluor 20×/0.45 objective lens (Nikon) and Magnafire digital charge-coupled device camera according to a standard protocol using the Osteomeasure Analysis System software (Osteometrics).

Statistical Methods

All of the data are presented as mean 6 SD or as mean followed by 95% confidence interval in parentheses. For statistical classification, a Student *t* test (2-tailed, unpaired) was performed using GraphPad Prism (GraphPad Software). Data comparisons were considered significant when P was less than 0.05.

RESULTS

^{64}Cu-RGD Uptake Is Increased in Tail Vertebrae of Tax$^+$ Mice with Osteolytic Lesions

Biodistribution studies were conducted on both Tax$^+$ and wild-type (WT) mice (Fig. 1B) by injecting ^{64}Cu-RGD via a femoral vein catheter, sacrificing the mice at 1 h after injection, excising organs of interest, and measuring the activity associated with those organs and tissues (Supplemental Figs. 1 and 2; supplemental materials are available online only at http://jnm.snmjournals.org). When the whole tail was excised and counted for activity, Tax$^+$ mice between the ages of 6 and 12 mo had significantly more radiopharmaceutical uptake in their tails than did age-matched WT control mice ($P = 0.013$). Tax$^+$ mice between the ages of 6 and 12 mo had an uptake range of 0.46–1.60 %ID/g, with a mean uptake of 1.034 ± 0.35 % ID/g, whereas WT mice between the ages of 6 and 12 mo showed uptake ranging from 0.11 to 1.04 %ID/g, with a mean of 0.71 ± 0.28 %ID/g. Tax$^+$ mice with well-established late-stage disease (>12 mo of age) were also evaluated. Tax$^+$ mice between the ages of 6 and 12 mo had significantly more activity associated with the whole tail than did Tax$^+$ mice older than 12 mo ($P = 0.003$) (Fig. 2A), whereas Tax$^+$ mice older than 12 mo had uptake of 0.38–0.59 %ID/g, with a mean activity of 0.47 ± 0.075 %ID/g. Conversely, when the activity associated with the tails of WT mice between the ages of 6 and 12 mo is compared with that of WT mice that are older than 12 mo, no significant difference in activity uptake is observed (Fig. 2B). Finally, to demonstrate that the radiotracer uptake is specific to osteolytic bone tumors, radiopharmaceutical uptake was measured in the liver tissue of these animals, because it should be devoid of osteoclasts. No significant differences in radiopharmaceutical uptake were observed between Tax$^+$ and WT mouse liver samples (Supplemental Fig. 2).

Serum TRAP analysis, an established measure of functional osteoclasts, was conducted on mice used in the biodistribution studies, and the results of this analysis are shown in Figure 2C. The values obtained from the analysis ranged from 0.17 to 0.54 U/L, with a mean value of 0.30 ± 0.11 U/L. These data demonstrate a correlation between the uptake of ^{64}Cu-RGD in the tails of Tax$^+$ mice and serum TRAP levels, suggesting that ^{64}Cu-RGD uptake in tumor-bearing tails was related to serum levels of osteoclast activity. There was no correlation between uptake of ^{64}Cu-RGD in WT tails and serum TRAP in the WT mice (Fig. 2D).

Small-Animal PET/CT Demonstrates ^{64}Cu-RGD Uptake at Osteolytic Lesions and at Sites of Osteoclast Recruitment

Small-animal PET/CT was also conducted to assess whether the radiopharmaceutical could enhance the visualization of active osteolysis and its associated inflammation in the vertebrae of Tax$^+$ mouse tails. Tax$^+$ and WT mice imaged 1 h after injection demonstrated radiopharmaceutical accumulation in their tail vertebrae (Figs. 3A and 4A). Areas of uptake were observed in tumors in the tail vertebrae of Tax$^+$ mice, but because Tax$^+$ tumor cells do not express β_3 integrin, radiopharmaceutical uptake in these tail vertebrae are not expected to be associated with Tax$^+$ tumor cells (14,20,28). SUVs were determined for the whole tails of both groups of animals. Tax$^+$ mice had approximately a 2-fold increase in tail-associated activity when compared with WT animals ($P = 0.016$) (Fig. 3B). Tax$^+$ tail SUVs ranged from 0.19 to 0.39, with an average whole-tail SUV of 0.28 ± 0.039; SUVs for WT tails ranged from 0.068 to 0.20, with an average SUV of 0.13 ± 0.028. Histologic analyses of vertebral bones demonstrate tumor infiltration of marrow with significant recruitment of TRAP$^+$ osteoclasts

at the tumor bone interface in Tax^+ mice (Fig. 4B) and demonstrate that areas of upregulated osteoclast recruitment can be distinguished from normal bone physiology using ^{64}Cu-RGD and small-animal PET/CT.

Small-Animal PET/CT Demonstrates ^{64}Cu-RGD Has Potential to Be Used to Monitor Bisphosphonate Therapy

Proof-of-principle small-animal PET/CT was conducted to assess whether the ^{64}Cu-RGD could be used to monitor response to standard bone-targeting osteoclast inhibition therapy in the vertebrae of Tax^+ mouse tails. Tumor-bearing Tax^+ mice were imaged with ^{64}Cu-RGD before and after treatment with ZA. Figure 5A represents the tail of a Tax^+ mouse before (left panel; SUV, 0.47) and after (right panel; SUV, 0.13) treatment with ZA. SUV analysis was applied to monitor radiopharmaceutical uptake in individual vertebrae (Fig. 5B). SUVs were calculated for the proximal and distal vertebra separated by this tumor. The proximal vertebra had an SUV of 0.38, which decreased to 0.12 after treatment. Similarly, the SUV of the distal vertebra before treatment was 0.43, whereas after treatment it decreased to 0.12. This demonstrates that ^{64}Cu-RGD is sensitive enough to detect changes in osteoclast activity induced by standard bone-targeting osteoclast inhibition therapy.

DISCUSSION

The goal of this work was to image the osteolytic component of bone metastasis and its associated inflammation in transgenic Tax^+ mice, a model of HTLV-1 adult T-cell leukemia and osteolytic bone disease (24) using PET and ^{64}Cu-RGD. This radiotracer is a specific ligand for the $\alpha_v\beta_3$ integrin, which is abundantly expressed on osteoclasts and inflammatory cells in the bone environment (20). Gao et al. noted that 86% of Tax^+ mice that developed soft-tissue tumors had radiographic evidence of osteolytic bone destruction that was observed before those soft-tissue tumors (29). Consequently, the Tax transgenic mouse model represents the first animal model of high-penetrance spontaneous osteolytic bone metastasis, which has come to illustrate the critical role of nonmalignant host and inflammatory cells that are recruited by tumor cells in the process of cancer progression and metastasis (29). Since Tax-induced disease arises spontaneously and occurs with greater frequency with age, biodistribution studies were undertaken using Tax^+ and WT mice in the following age groups: Tax^+ mice 6–12 mo old, Tax^+ mice more than 12 mo old, WT mice 6–12 mo old, and WT mice more than 12 mo old. First, Tax^+ mice between the ages of 6 and 12 mo have significantly higher uptake of the radiopharmaceutical in the tail vertebrae than do the WT mice of the same age range, but this difference in uptake is not observed in tissues that would not suffer from osteolytic bone disease.

Radiotracer uptake is different in Tax^+ mice of different age groups. For example, uptake of the radiopharmaceutical in the tail was significantly greater in Tax^+ mice between the ages of 6 and 12 mo than in Tax^+ mice older than 12 mo, but there were no age-related differences in tail uptake in WT mice. This change in radiopharmaceutical uptake may reflect a difference in the severity of the pathology associated with Tax expression. Increased uptake of radioactivity in Tax^+ mice at 6–12 mo reflects mice with active osteolytic bone disease and its associated inflammation, whereas those mice older than 12 mo that have less radiopharmaceutical uptake in their tails reflect a less severe form of the disease. These observations are in agreement with what has been reported previously by Gao (29) and resembles the clinical presentation of patients who have radiographic evidence of osteolytic bone metastases but whose lesions are inactive. This condition provides a preclinical example of how this radiopharmaceutical can be used as a diagnostic tool by physicians to stage more accurately the extent of the osteolytic disease and its progression while enabling the clinician to prescribe a more accurate course of treatment based on the results obtained using this tracer.

Small-animal PET/CT was also conducted on the tails of Tax^+ and WT mice and corroborated the results of biodistribution studies but provided more complete data with respect to determining the specific areas of focal tracer uptake. The Tax^+ mice develop osteolytic lesions in their hind limbs and tail. The tail was chosen for imaging for practical reasons, primarily because it is easy to repeat studies and get the tail in approximately the same position. Additionally, the bladder activity does not interfere as much with the tail as do the hind limbs. For example, Figures 3A and 4A show high focal ^{64}Cu-RGD uptake in specific vertebra of the Tax^+ mouse tail, suggesting that there is specific uptake where there is the greatest amount of bone destruction and, hence, tumor-recruited osteoclasts. The overall data from small-animal PET/CT studies show that radiopharmaceutical uptake is higher in the tails of Tax^+ mice than in the tails of WT mice (Fig. 3B). This increase in the Tax^+ mouse tail SUV, when compared with that of WT mice, suggests that the radiopharmaceutical is able to distinguish between the osteolytic disease state observed in the Tax^+ mouse tail vertebra and the normal bone physiology occurring in the WT mouse vertebra. Previously, Sprague et al. demonstrated that osteoclasts expressing high levels of $\alpha_v\beta_3$ integrin could be imaged using ^{64}Cu-RGD in a pharmacologically induced model of osteolysis and that the targeting of osteoclasts could be blocked by the coinjection of c(RGDyK), suggesting that uptake of the radiopharmaceutical by osteoclasts is mediated by integrin $\alpha_v\beta_3$ binding (20). In addition, osteolytic bone lesions of Tax^+ mice are observed to contain neutrophils, which have been shown to express $\alpha_v\beta_3$ (30). Because osteoclasts, neutrophils, and lymphocytes will express the $\alpha_v\beta_3$ integrin, the radiopharmaceutical is believed to bind to the integrin on all 3 cell types, and this binding is responsible for the selective uptake within the Tax^+ mouse vertebra and results in the enhanced signal when compared with the accumulated activity associated with the tails of WT mice. Interestingly, the soft-tissue tumors observed on the tails of Tax^+ mice were also observed to have tracer uptake. However, because Tax^+ tumor cells lack the β_3 integrin (X. Xu and K. Weilbaecher, unpublished data), the radiopharmaceutical is most likely binding to the inflammatory cells within the tumor in addition to neovasculature associated with the blood supply of the tumor (30).

Nitrogen-containing bisphosphonates such as ZA have been observed to decrease osteoclast number, osteoclast activation, and bone desorption by induction of osteoclast apoptosis (31). Bisphosphonates are believed to inhibit the farnesyl diphosphate synthase in the mevalonate pathway and thereby prevent the protein prenylation of small GTPase-signaling proteins required for osteoclast function (32). Preliminary data using small-animal imaging and SUV analysis suggest that the radiopharmaceutical ^{64}Cu-RGD can be used to monitor bisphosphonate therapy because of the ability of this agent to image osteoclasts by targeting the $\alpha_v\beta_3$ integrin. Radiopharmaceutical uptake was analyzed either by drawing regions of interest on the entire tail portion of the vertebral column or by analyzing specific areas of increased uptake in individual vertebrae. When measured by SUV analysis, activity was seen to decrease in the whole tail or individual vertebrae after bisphosphonate therapy. Because bisphosphonates are believed to induce osteoclast apoptosis, the decrease in uptake is attributed to decreased numbers of osteoclasts within the bone microenvironment. This result suggests that ^{64}Cu-RGD is sensitive enough to detect decreased numbers of osteoclasts. ZA treatment also resulted in a decrease in the tumor SUV from 0.51 before therapy to 0.26 after therapy. This decrease was expected because the pharmacology of bisphosphonates has been demonstrated to induce apoptosis in other cell types besides osteoclasts (31).

When histology is conducted on tails imaged using small-animal PET/CT, Tax^+ tumor cells and nonmalignant inflammatory cell such as neutrophils and lymphocytes are observed within the bone microenvironment. Moreover, at the tumor–bone interface, osteoclasts are present in resorptive pits, indicating active bone resorption. The histologic evidence corroborates results from biodistribution and small-animal imaging experiments and supports the hypothesis that

differences in radiopharmaceutical uptake are due to increases in the number of osteoclasts and inflammatory cells within the vertebrae of Tax^+ mouse tails.

CONCLUSION

The radiopharmaceutical ^{64}Cu-RGD was evaluated as an imaging agent for osteolytic bone metastases and their associated inflammation in the Tax^+ mouse model by targeting the $\alpha_v\beta_3$ integrin on osteoclasts and the proinflammatory cells involved at the metastatic site. Tax^+ mice between the ages of 6 and 12 mo had significantly more activity associated with the tail tissue than did Tax^+ mice older than 12 mo and WT control mice of the same age range. Small-animal PET/CT demonstrated greater radiopharmaceutical uptake in the tails of Tax^+ mice and demonstrated that this radiopharmaceutical can be used to monitor bisphosphonate therapy. Histologic analysis of Tax^+ mouse tail vertebrae revealed that Tax^+ tumor cells, osteoclasts, and proinflammatory cells were also observed within the bone microenvironment, corroborating the small-animal imaging results and suggesting that 64Cu-RGD has the potential to be an effective imaging agent for osteolytic bone metastases.

Supplementary Material

Refer to Web version on PubMed Central for supplementary material.

Acknowledgments

We acknowledge Dr. Riccardo Ferdani for synthesis of CB-TE2A, Drs. Samuel Achilefu and Yunpeng Ye for synthesis of the CB-TE2A-c(RGDyK) conjugate, Christopher Sherman for technical assistance, Drs. Zhying Xu and Özge Uluckan for assistance with the animal model, and Crystal Darby for expert histologic sample preparation. We gratefully acknowledge NIH grants F32 CA115148, R21 CA098698, R24 CA86307 (production of ^{64}Cu at Washington University School of Medicine), P30 CA91842 (Alvin J. Siteman Cancer Center at Washington University in St. Louis), P01 100730, and the Department of Defense Breast Cancer Research Program grant W81XWH-04-1-0396.

REFERENCES

1. Mundy GR. Metastasis to bone: causes, consequences and therapeutic opportunities. Nat Rev Cancer 2002;2:584–593. [PubMed: 12154351]
2. Hamaoka T, Madewell JE, Podoloff DA, Hortobagyi GN, Ueno NT. Bone imaging in metastatic breast cancer. J Clin Oncol 2004;22:2942–2953. [PubMed: 15254062]
3. Hsu WK, Virk MS, Feeley BT, Stout DB, Chatziioannou AF, Lieberman JR. Characterization of osteolytic, osteoblastic, and mixed lesions in a prostate cancer mouse model using ^{18}F-FDG and ^{18}F-fluoride PET/CT. J Nucl Med 2008;49:414–421. [PubMed: 18287261]
4. Bombardieri E, Crippa F. PET imaging in breast cancer. Q J Nucl Med 2001;45:245–256. [PubMed: 11788817]
5. Cook GJ, Fogelman I. The role of positron emission tomography in the management of bone metastases. Cancer 2000;88:2927–2933. [PubMed: 10898336]
6. Moon DH, Maddahi J, Silverman DH, Glaspy JA, Phelps ME, Hoh CK. Accuracy of whole-body fluorine-18-FDG PET for the detection of recurrent or metastatic breast carcinoma. J Nucl Med 1998;39:431–435. [PubMed: 9529287]
7. Liu W, Hajibeigi A, Lin M, et al. An osteoclast-targeting agent for imaging and therapy of bone metastasis. Bioorg Med Chem Lett 2008;18:4789–4793. [PubMed: 18692394]
8. Bhushan KR, Tanaka E, Frangioni JV. Synthesis of conjugatable bisphosphonates for molecular imaging of large animals. Angew Chem Int Ed Eng 2007;46:7969–7971.
9. Kumar S, Dare L, Vasko-Moser JA, et al. A highly potent inhibitor of cathepsin K (relacatib) reduces biomarkers of bone resorption both in vitro and in an acute model of elevated bone turnover in vivo in monkeys. Bone 2007;40:122–131. [PubMed: 16962401]

10. Kim MK, Kim HD, Park JH, et al. An orally active cathepsin K inhibitor, furan-2-carboxylic acid, 1-{1-[4-fluoro-2-(2-oxo-pyrrolidin-1-yl)-phenyl]-3-oxo-piperidin-4-ylcarbamoyl}-cyclohexyl-amide (OST-4077), inhibits osteoclast activity in vitro and bone g loss in ovariectomized rats. J Pharmacol Exp Ther 2006;318:555–562. [PubMed: 16699068]
11. Tanaka S, Nakamura K, Oda H. The osteoclast: a potential therapeutic target of bone and joint destruction in rheumatoid arthritis. Mod Rheumatol 2001;11:177–183.
12. Nicholson GC, Malakellis M, Collier FM, et al. Induction of osteoclasts from CD14-positive human peripheral blood mononuclear cells by receptor activator of nuclear factor κB ligand (RANKL). Clin Sci 2000;99:133–140. [PubMed: 10918046]
13. Hua J, Dobrucki LW, Sadeghi MM, et al. Noninvasive imaging of angiogenesis with a ^{99m}Tc-labeled peptide targeted at $\alpha_v\beta_3$ integrin after murine hindlimb ischemia. Circulation 2005;111:3255–3260. [PubMed: 15956134]
14. Jin H, Varner J. Integrins: roles in cancer development and as treatment targets. Br J Cancer 2004;90:561–565. [PubMed: 14760364]
15. Bakewell SJ, Nestor P, Prasad S, et al. Platelet and osteoclast β_3 integrins are critical for bone metastasis. Proc Natl Acad Sci USA 2003;100:14205–14210. [PubMed: 14612570]
16. Clezardin P. Recent insights into the role of integrins in cancer metastasis. Cell Mol Life Sci 1998;54:541–548. [PubMed: 9676573]
17. Chen X, Liu S, Hou Y, et al. MicroPET imaging of breast cancer α v-integrin expression with ^{64}Cu-labeled dimeric RGD peptides. Mol Imaging Biol 2004;6:350–359. [PubMed: 15380745]
18. Chen X, Park R, Shahinian Anthony H, et al. ^{18}F-labeled RGD peptide: initial evaluation for imaging brain tumor angiogenesis. Nucl Med Biol 2004;31:179–189. [PubMed: 15013483]
19. Chen X, Sievers E, Hou Y, et al. Integrin $\alpha_v\beta_3$-targeted imaging of lung cancer. Neoplasia 2005;7:271–279. [PubMed: 15799827]
20. Sprague JE, Kitaura H, Zou W, et al. Noninvasive imaging of osteoclasts in parathyroid hormone-induced osteolysis using a ^{64}Cu-labeled RGD peptide. J Nucl Med 2007;48:311–318. [PubMed: 17268030]
21. Qaim SM, Bisinger T, Hilgers K, Nayak D, Coenen HH. Positron emission intensities in the decay of copper-64, bromine-76 and iodine-124. Radiochim Acta 2007;95(2):67–73.
22. McCarthy DW, Shefer RE, Klinkowstein RE, et al. The efficient production of high specific activity Cu-64 using a biomedical cyclotron. Nucl Med Biol 1997;24:35–43. [PubMed: 9080473]
23. Weisman GR, Rogers ME, Wong EH, Jasinski JP, Paight ES. Cross-bridged cyclam. protonation and Li^+ complexation in a diamond-lattice cleft. J Am Chem Soc 1990;112:8604–8605.
24. Grossman WJ, Kimata JT, Wong F-H, Zutter M, Ley T, Ratner L. Development of leukemia in mice transgenic for the tax gene of human T-cell leukemia virus type I. Proc Natl Acad Sci USA 1995;92:1057–1061. [PubMed: 7862633]
25. Wadas TJ, Anderson CJ. Radiolabeling of TETA- and CB-TE2A-conjugated peptides with copper-64. Nat Protoc 2007;1:3062–3068. [PubMed: 17406569]
26. Boswell CA, Sun X, Niu W, et al. Comparative in vivo stability of copper-64-labeled cross-bridged and conventional tetraazamacrocyclic complexes. J Med Chem 2004;47:1465–1474. [PubMed: 14998334]
27. Sun X, Wuest M, Weisman Gary R, et al. Radiolabeling and in vivo behavior of copper-64-labeled cross-bridged cyclam ligands. J Med Chem 2002;45:469–477. [PubMed: 11784151]
28. Hendey B, Lawson M, Marcantonio EE, Maxfield FR. Intracellular calcium and calcineurin regulate neutrophil motility on vitronectin through a receptor identified by antibodies to integrins α_v and β_3. Blood 1996;87:2038–2048. [PubMed: 8634455]
29. Gao L, Deng H, Zhao H, et al. HTLV-1 Tax transgenic mice develop spontaneous osteolytic bone metastases prevented by osteoclast inhibition. Blood 2005;106:4294–4302. [PubMed: 16118323]
30. Horton MA. The $\alpha_v\beta_3$ integrin "vitronectin receptor.". Int J Biochem Cell Biol 1997;29:721–725. [PubMed: 9251239]
31. Padalecki SS, Guise TA. Actions of bisphosphonates in animal models of breast cancer. Breast Cancer Res 2002;4:35–41. [PubMed: 11879558]

32. Russell RGG, Xia Z, Dunford JE, et al. Bisphosphonates: an update on mechanisms of action and how these relate to clinical efficacy. Ann N Y Acad Sci 2007;1117:209–257. [PubMed: 18056045]

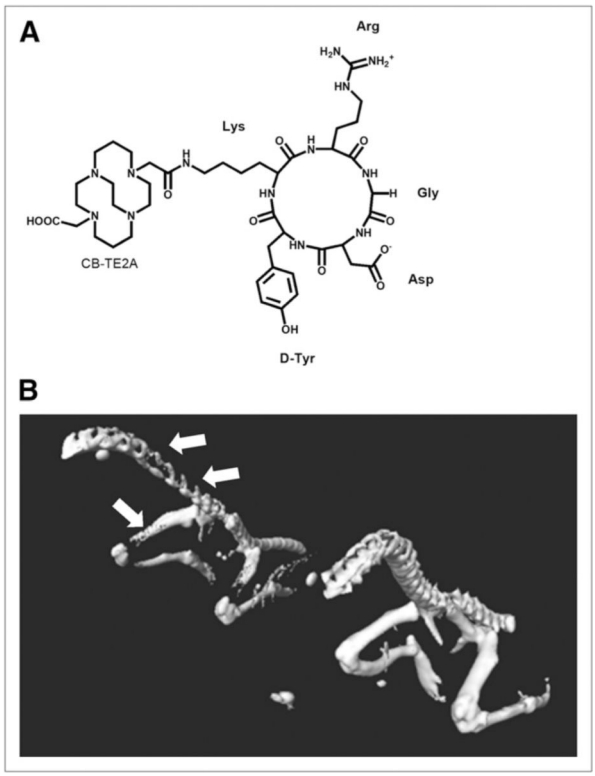

FIGURE 1.

(A) Structure of CB-TE2A-c(RGDyK). (B) Isosurface image rendered from high-resolution CT data collected on Tax^+ and WT mice. Isosurface images are rendered using same parameters and are equivalent. Arrows depict sites of osteolytic bone destruction in spinal vertebrae and femur of Tax^+ mouse.

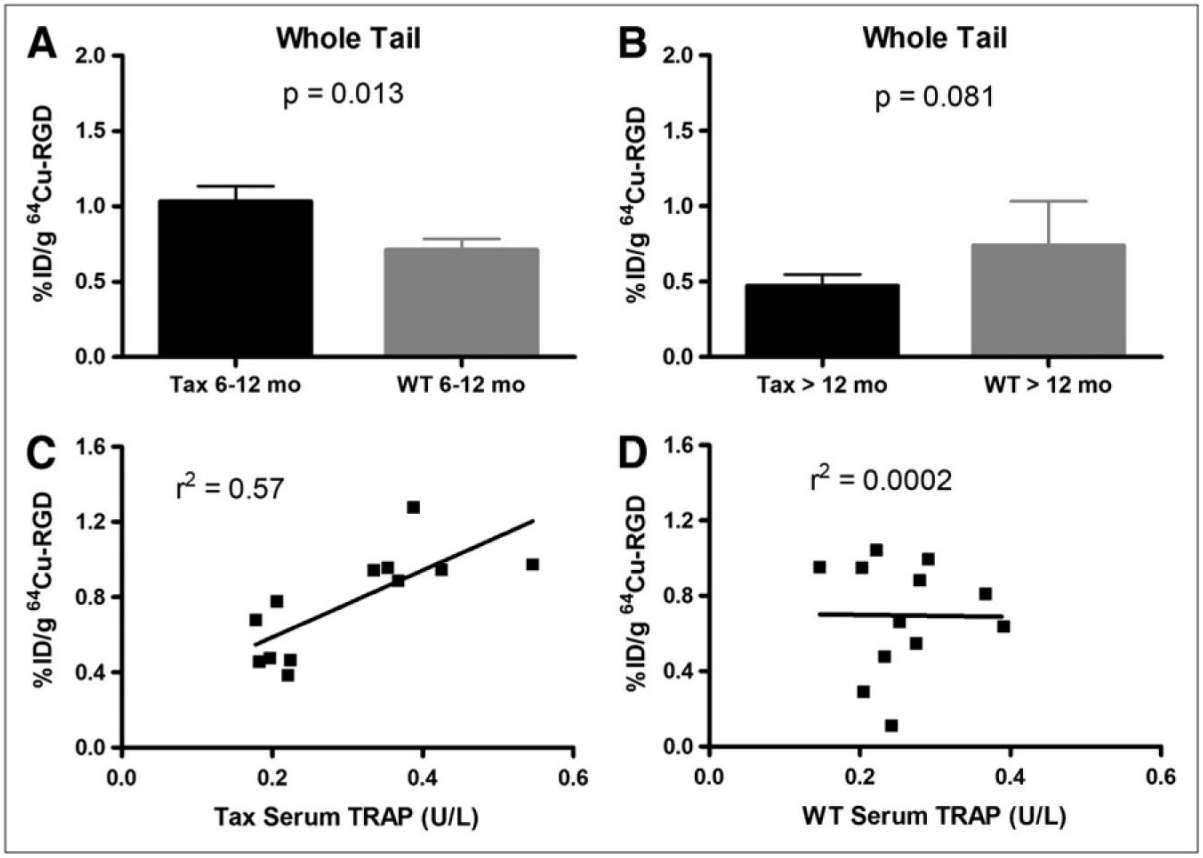

FIGURE 2.

Biodistribution of ^{64}Cu-RGD is different in Tax$^+$ and WT mice. (A) Statistically significant differences are observed between accumulation of radioactivity in tails of 6- to 12-mo-old Tax$^+$ (n = 12) and WT mice (n = 15). Additionally, uptake of ^{64}Cu-RGD in 6- to 12-mo-old Tax$^+$ mice is higher than in those older than 12 mo (P = 0.003). (B) However, statistically significant differences are not observed when radiopharmaceutical accumulation in tails of Tax$^+$ mice that are older than 12 mo (n = 5) is compared with radiopharmaceutical accumulation in tails of WT mice in same age range (n = 6). (C) Positive correlation exists between accumulated tracer uptake in Tax$^+$ mouse tails and measured serum TRAP levels in blood of these mice. High degree of variability reflects spontaneous nature of animal model. (D) Conversely, no correlation exists between accumulated tracer uptake in WT mouse tails and measured serum TRAP levels in blood of WT mice. Sera from both age groups were combined in parts C and D.

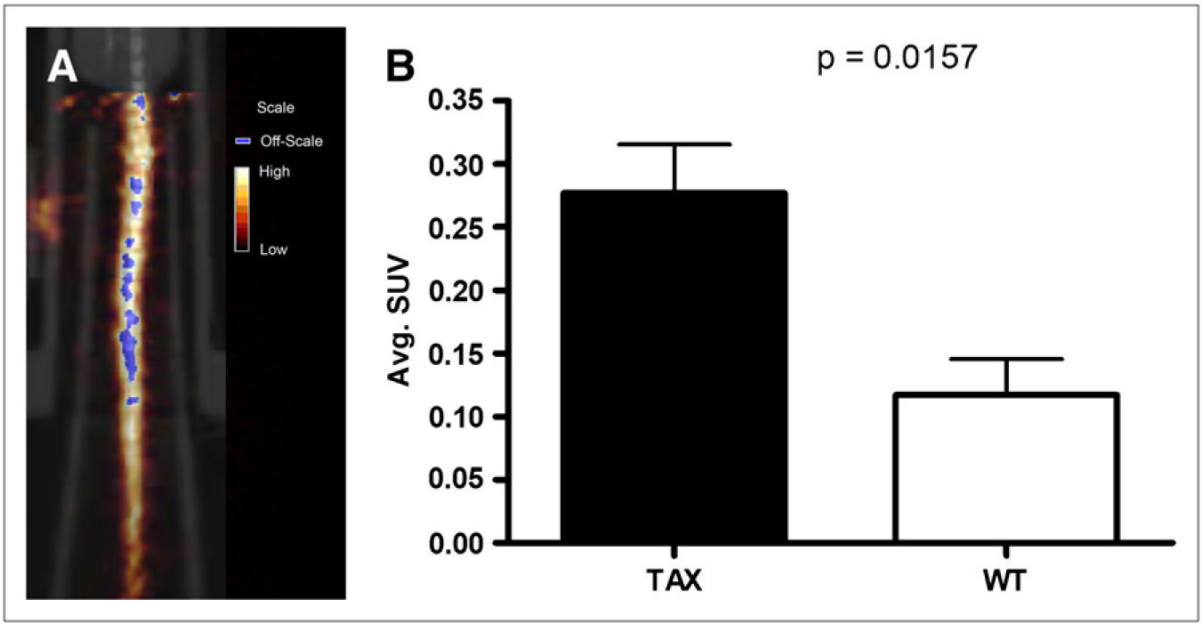

FIGURE 3.

(A) Coregistered small-animal PET/CT image of Tax^+ mouse tail that was imaged with ^{64}Cu-RGD at 1 h after injection. Coronal slice presented here has numerous areas of focal uptake in tail vertebrae. (B) Graphic representation of observed differences in SUV between Tax^+ (n = 5) and WT (n = 4) mice. On basis of SUV analysis, more activity is observed in Tax^+ mouse tails.

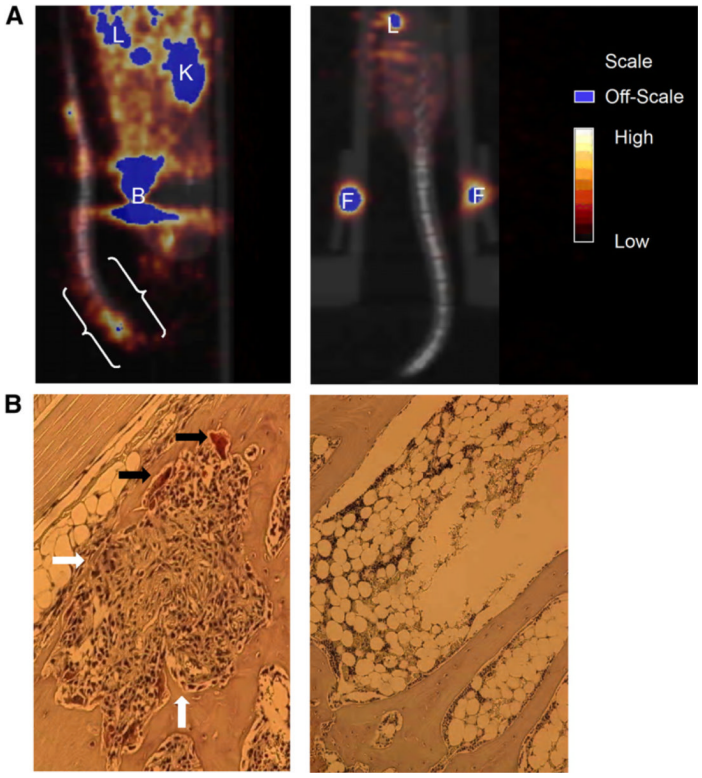

FIGURE 4.

(A) Coregistered small-animal PET/CT images of Tax$^+$ and WT mice (both 14 mo old) at 1 h after injection. OSEM reconstructions were used here, and only lower body of each mouse was placed in field of view. (A, left image) Sagittal slice of Tax$^+$ mouse tail, which was held in place such that tail looped up onto ventral side of mouse. White brackets indicate where histologic sectioning was conducted. (A, right image) Coregistered small-animal PET/CT image (coronal slice) of WT mouse. Little activity is observed in tail vertebrae of this mouse. (B, left image) TRAP-stained section from tail of Tax$^+$ mouse shown in A, which depicts osteolytic lesion. Several osteoclasts are indicated by black arrows, whereas tumor and proinflammatory cell infiltration is indicated by white arrows. (B, right image) TRAP-stained section from tail of WT mouse. Osteoclasts and proinflammatory cells are not observed in healthy marrow. B = bladder; F = fiducial marker; K = kidney; L = liver.

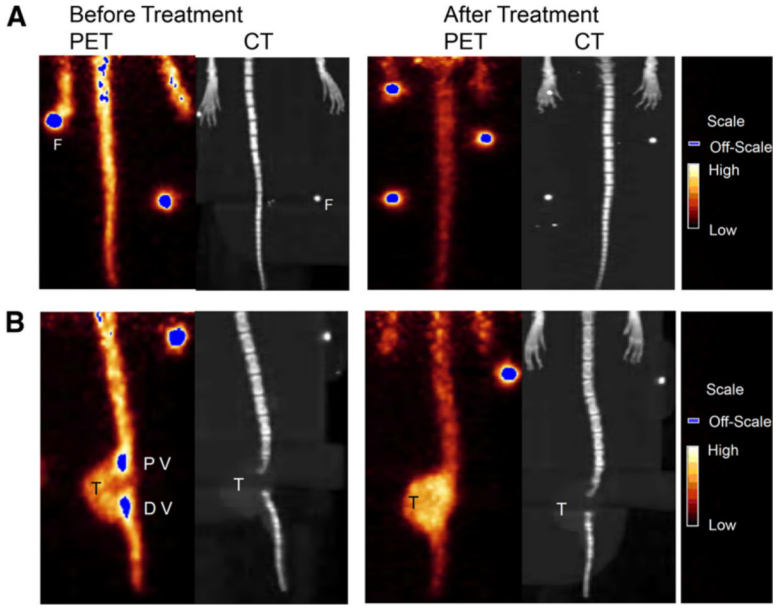

FIGURE 5.

Small-animal PET/CT (with ^{64}Cu-RGD) results before (left) and after (right) treatment with ZA. Three animals were used in this proof-of-principle study. Small-animal CT and small-animal PET data were rendered as whole-body reprojected images, which were summations of individual data slices. Notably, changes in bone due to administered therapy are observed in small-animal PET before being observed in the small-animal CT and can be quantified by determining SUVs before and after therapy. (A) Tax$^+$ mouse tail demonstrates appreciable radiopharmaceutical uptake at time of imaging. SUV for whole tail of this animal before treatment was 0.47, but after therapy it was 0.13. (B) Different Tax$^+$ mouse tail has developed large soft-tissue tumor. Here SUV analysis was conducted on 2 vertebrae separated by tumor. Before therapy, proximal vertebra (PV) and distal vertebra (DV) had SUVs of 0.38 and 0.43, respectively. After treatment with ZA, SUV of PV was 0.12 and SUV of DV was 0.12. F = fiducial marker; T = tumor.